A comparative study on the properties of $Er_xZn_{1-x}O$ and $Sm_xZn_{1-x}O$ nanostructured thin films for electronic device applications

Justine S. Nyarige[a], Fredjoe Nambala[a b], Mmantsae Diale[a*]

[a]Department of Physics, University of Pretoria, Private Bag X20, Hatfield 0028, South Africa

[b]Department of Physics, University of Zambia, PO Box 32379, Great East Road Campus, Lusaka, Zambia

Correspondence author's email and phone number: mmantsae.diale@up.ac.za, +27124204418

Abstract

In this study, the undoped, Erbium (Er) doped and Samarium (Sm) doped (1, 3, and 5 wt%) ZnO were synthesized using spray pyrolysis. X-ray diffraction patterns confirmed ZnO with strong diffraction peaks indexed in their right 2-theta angles. Raman spectroscopy observed A_1, E_1 and E_2 vibrational phonon modes of wurtzite hexagonal ZnO. Scanning electron microscopy revealed nanoparticles that were well dispersed on the surface. There was agglomeration which was decreasing with an increase in the doping concentration from 1 to 5 wt% of Er and Sm. Energy-dispersive X-ray spectroscopy confirmed the main signals for Zn, O, Er, and Sm, with no other foreign elements observed. From the UV-Vis measurements, average transmittance of 74 % at 550 nm was obtained for all the samples. The bandgap calculated for the thin films was decreasing from 3.31 eV for undoped ZnO to 2.96 eV and 3.11 eV for 5% Er and Sm doped samples, respectively. Schottky diodes were fabricated using aluminum (Al) and gold (Au) as the Schottky contact and palladium (Pd) as the Ohmic contact and electrical measurements performed. Both undoped and doped ZnO showed a rectifying behavior with an improvement in the rectification of up to almost 4 orders of magnitude for 5 wt% Er and Sm doped films compared to undoped ZnO which had a rectification of 2. In addition, the Schottky Barrier heights increased from 0.559 for undoped ZnO to 0.767 and 0.760 for 5 wt% Er and Sm doped, respectively. Undoped ZnO had an ideality factor of 2.49 which was decreased to 1.72 and 1.92 for Er and Sm doped ZnO devices. Also, a reduction in the leakage current and series resistance of devices was noted in undoped and doped ZnO. The fabricated devices can be used as an alternative for Schottky diode applications.

Keywords. Zinc oxide, doping, samarium, erbium, Schottky barrier heights

1. Introduction

Metal oxide semiconductors have been a subject of intensive investigations over the last decades due to their fascinating properties and versatile applications in optoelectronics [1]. Among these semiconductors, Zinc oxide (ZnO) is the most widely studied semiconductor. ZnO, a II-VI semiconductor, has been used in many applications such as a photocatalyst [2], optoelectronics [3], gas sensing [4], and water filtration [5] due to its wide bandgap of 3.37 eV and high exciton binding energy of 60 meV [6]. In addition, ZnO is non-toxic and has high transparency in the visible region [7]. ZnO has also been used in solar-blind photodetectors such as metal-semiconductor photodetectors [8] and Schottky barrier height photodetectors [9]. The interface between the metal and semiconductor plays a major role in the formation of these detectors, where there is a small leakage current for a large barrier height and a high breakdown voltage.

Several metals have been used in the fabrication of the Schottky-barrier diodes (SBD) with ZnO. For instance, a faster switching and low dark current are exhibited by the Schottky barrier photodetectors, leading to a controllable photo-detectable behavior compared to the non-rectifying junctions [10]. The oxygen vacancies which are the main defects in ZnO result in poor electrical properties due to the electron tunneling into the ZnO from the metal [11]. The electrical, structural, and optical properties of ZnO can be altered by doping with metals such as nickel (Ni), platinum (Pt), silver (Ag), gold (Au), just to mention a few [1, 7, 12, 13]. Rare earth (RE) metals have also been reported to improve the SBD of ZnO. This is due to their availability in the 4f orbitals and high fluorescence efficiencies, leading to better optical and electrical properties. Some of the reported transition metals include erbium (Er), samarium (Sm), cerium (Ce), and lanthanum (La) [14-16]. The nanostructured ZnO has been reported to produce better Schottky diodes compared to the bulk semiconductors.

Some of the nanostructured ZnO thin films that have been reported in SBD include nanorods [6], nanowires [17], nanotubes [18], nanobelts [19], and nanoparticles [20]. These nanostructures of ZnO have been grown using different methods. Methods such as chemical vapor deposition (CVD) [21], pulsed laser deposition (PLD) [22], chemical spray pyrolysis (CSP) [23], chemical bath deposition (CBD) [24], sol-gel spin coating [25], hydrothermal [26], electrodeposition [27], and dip-coating [28] have been used in the preparation of nanostructured ZnO thin films. Of these methods, spray pyrolysis was preferred in the preparation of ZnO nanoparticles in this study. Some

of the merits of the method include easy to set-up, different parameters like the deposition time, substrate to nozzle distance, and deposition can be varied, giving different stoichiometry of the prepared films [3]. Different materials have been used as Schottky and Ohmic contacts.

The rectification of the SBD varies depending on the materials used. For example, SBD using palladium (Pd) as Schottky and indium doped tin oxide (ITO) Ohmic contacts, respectively have been reported on ZnO doped with Ce, Er and Sm [29]. Gold-antimony (Au-Sb) alloy has also been used as the Schottky contact, with Pd as Ohmic contact as reported by Ahmed *et. al* [14]. In most of these studies, the Schottky and Ohmic contacts have been deposited at the back and in front of the substrate, respectively. Not many studies have reported the electrical properties of ZnO where the Schottky and Ohmic contacts are deposited on top of the ZnO layer. Further, even though the electrical properties of individual doping of Sm and Er has been reported by other researchers, a comparative study of the behavior of ZnO doped with Er and Sm (Er_xZnO_{1-x} and Sm_xZnO_{1-x}) films has not been fully explored. Also, the electrical properties of undoped, Er-doped and Sm-doped ZnO using Al-Au as Schottky contacts and Pd as Ohmic contacts have not been reported hence the motivation for performing this experiment.

In this study, undoped ZnO, Er_xZnO_{1-x} and Sm_xZnO_{1-x} nanostructured films were prepared using chemical spray pyrolysis at an optimized deposition temperature of 400ºC and structural, morphological and optical properties studied. Schottky and Ohmic contacts were deposited on the ZnO layer to study the electrical properties. An improvement of rectification of the order of about 4 for the 5 wt % of Sm and Er-doped devices compared to undoped ZnO that had a rectification of order 2.

Experimental

2.1 Substrate cleaning

The silicon wafer and soda-lime glass were used as substrates in this experiment. The p-silicon (p-Si) wafers were placed in beakers containing tetrachloro-ethylene, acetone and methanol followed by ultra-sonication for about 10 min in each step. These wafers were rinsed with deionized (DI) water. The substrates were thereafter etched by dipping them in a beaker containing 2 % hydrofluoric acid (HF) for 60 s and finally rinsed with DI water. For the soda-lime glass, the

substrates were soaked in a beaker containing detergent and sodium hydroxide for 15 min. This was followed by rinsing with DI water. The rinsed substrates were later transferred to beakers containing ethanol, and acetone and ultra-sonicated for 5 min, rinsing with DI water in each step. The substrates were blown to dry using nitrogen gas.

2.2 Sample preparation

Zinc acetate dihydrate ($C_4H_{12}O_6Zn.2H_2O$, Sigma Aldrich-South Africa, 99.99%), erbium (III) nitrate pentahydrate $Er(NO_3)_3.5H_2O$, Sigma Aldrich-South Africa, 99.99 %) samarium (III) nitrate hexahydrate $Sm(NO_3)_3.6H_2O$ Sigma Aldrich-South Africa, 99.99%) were used as received without further purification. Chemical spray pyrolysis adopted from our previous work [30-32] was used in the deposition of undoped and doped ZnO. 50 mM of $C_4H_{12}O_6Zn.2H_2O$ was dissolved in 100 mL of DI water, and the solution was mixed at a temperature of 35 ºC for 10 min. The precursor was used to prepare undoped ZnO films at a deposition temperature of 400 ºC, and a deposition time of 30 s. The solutions of 1 wt% of the $Er(NO_3)_3$ and $Sm(NO_3)_3$ were prepared separately in beakers containing 10 mL of DI water. The solution was then added to the 50 mM of ZnO precursor in separate beakers and stirred copiously using a magnetic bead for 5 min. The precursors were later deposited on p-Si and soda-lime glass substrates using spray pyrolysis with the optimized parameters (400 ºC and 30 s deposition time). The experiment was repeated for 3wt% and 5 wt% of $Er(NO_3)_3$ and $Sm(NO_3)_3$. The samples were annealed at 500 ºC for 1 h and left to cool naturally to room temperature. The undoped, Er_xZnO_{1-x} and Sm_xZnO_{1-x} were annealed separately in the furnace to avoid contamination.

The glass and p-Si samples were prepared under the same conditions. Samples prepared on glass were used to study the structural, morphological and optical properties while samples prepared on p-Si were used for electrical characterization. Before the deposition of the contacts, half the surface area of the ZnO films was used in the deposition of Schottky while the other half was for Ohmic contacts. The Al foil was used to cover the half samples before beginning the deposition process. The Schottky shadow mask was then placed on top of the samples before loading them into the system. 100 nm and 80 nm thick of Al and Au Schottky contacts with a diameter of 0.6 mm were evaporated on top of the ZnO layer using Edwards's thermal evaporation system. For the Ohmic contacts, a 100 nm thick of Pd were evaporated on the other half of the sample that was covered

initially by Al foil. The vacuum pressure used in the deposition of Ohmic and Schottky contacts was 5.5 x 10^{-6} mbar.

2. Characterization

The crystal structure of the undoped and doped ZnO thin films was studied using Bruker 2D Phaser X-ray Diffractometer (XRD) with CuK_{α} radiation, a 0.15418 nm source, 2θ ranging from 30 - 70º and a scanning rate of 0.02º. Raman spectroscopy was used to identify the lattice vibrational modes of ZnO before and after doping using a WITec alpha 300 RAS confocal Raman microscope with a 532 nm excitation laser. Field emission scanning electron microscope (Zeiss Ultra PLUS FESEM-Microscopes) operating at 2 kV was used to study the surface morphology of the thin films. Elemental analysis of the samples was performed using energy-dispersive X-ray (EDX) spectroscopy attached to SEM. Cary 60 UV-Vis was used to study the optical properties of the films that were deposited on glass substrates. Electrical measurements were performed using current-voltage (*I-V*) measurements at room temperature. Figure 1 presents the architecture of the samples used in electrical measurements.

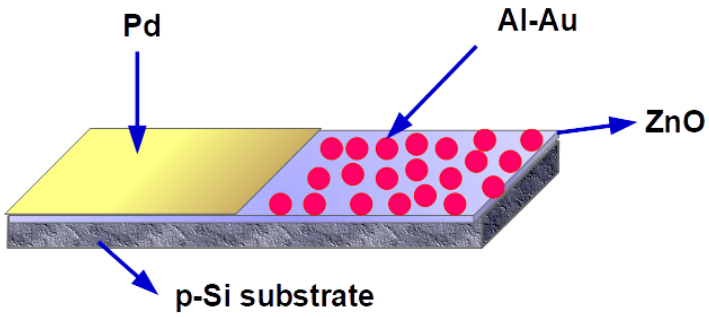

Figure 1. The architecture of ZnO with the Schottky (Al-Au) and Ohmic (Pd) contacts

2.1 Structural and morphological characterization

Figure 2 presents the XRD patterns of undoped ZnO, Er_xZnO_{1-x} and Sm_xZnO_{1-x}. The peaks for ZnO; (100), (002), (101), (102), (110), (103), (112) were indexed at 31.1º, 33.7º, 35.5º, 46.8º, 56.0º, 62.1º, 67.2º, respectively and corresponded to the JCPDS file # 36-1451. These peaks are associated with the wurtzite hexagonal structure of ZnO indexed in their right 2-theta angles, with

a (101) as the preferred orientation. From Figure 2, the intensity of undoped ZnO was relatively higher than the Er_xZnO_{1-x} and Sm_xZnO_{1-x} samples. The sharp peaks of (100), (002), and (101) revealed the polycrystalline nature of the prepared samples. Other peaks from the dopants were not present, an indication of the substitution with Zn^{2+} ions with Sm^{3+} and Er^{3+} after doping. There was an observed slight shift of the peaks to lower 2-theta angles for doped samples as compared to undoped ones. The shifting mainly occurs when the ionic radius of the dopant is larger than the one of the host. In this study, the ionic radius of Er and Sm was 0.88 Å and 0.94 Å. This was higher compared to the host (Zn^{2+}) which has an ionic radius of 0.74 Å [33].

ZnO has a high-intensity peak of the (002) plane, which is evident from Figure 2 for the undoped ZnO sample. This is a clear indication that there was low surface energy on the plane before doping [34]. For ZnO:Er, there was an increase in the peak intensity for all the planes. 5 % doped ZnO:Er revealed the highest intensity, an indication of improved crystallinity growth. However, this was not the case for ZnO:Sm samples, whereby there was a decrease in intensity. The decrease in the peak intensity at high doping concentration could be due to increased saturation of the new centers of nucleation [35]. A study by Li *et al.* on the doping and annealing effects of ZnO doped with cadmium revealed that the decrease of the (002) peak maybe be affected by saturation of the newer nucleation centers and amorphous cadmium components segregation [36].

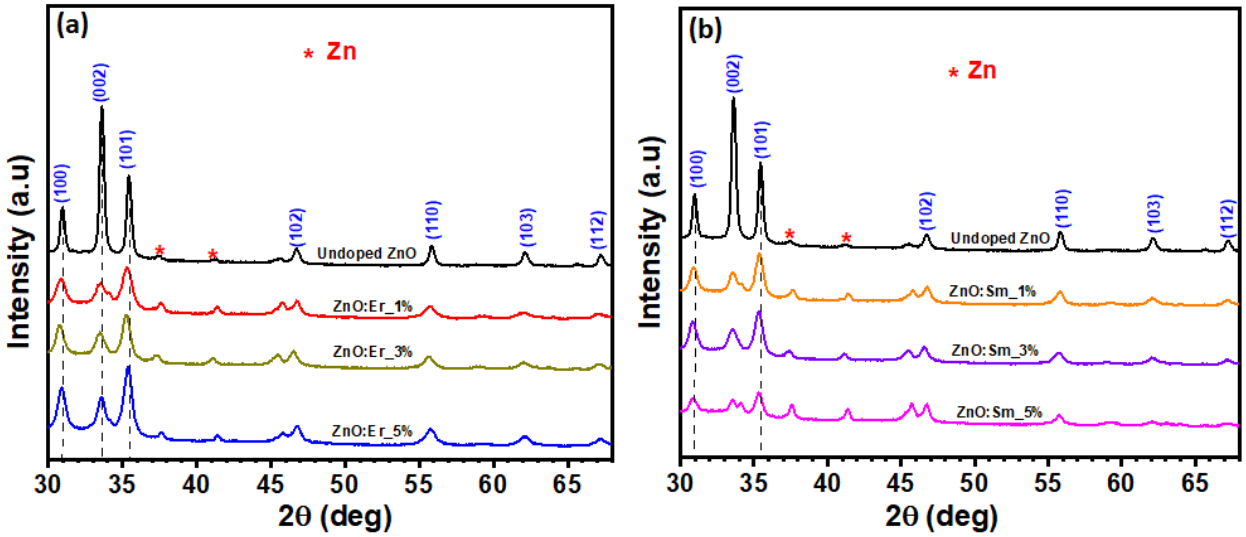

Figure 2. X-ray diffraction of undoped ZnO, ZnO:Er and ZnO**:**Sm thin films

The crystallite sizes of the films were calculated using Debye-Scherrer's equation;

$$D = \frac{k\lambda}{\beta cos\theta} \quad (1)$$

while the lattice strain was obtained using;

$$\varepsilon = \frac{\beta}{4tan\theta} \quad (2)$$

where D, β, λ and θ are the average crystallite size, angular peak width at half maximum in radians, wavelength (0.15418 nm) and Bragg angle, respectively. Figure 3 presents the calculated crystallite sizes and strain for undoped and doped ZnO thin films that were obtained by averaging the (100), (002), and (101) which were the most intense peaks.

There was an observed decrease in the crystallite size with the increase in doping concentration for the ZnO:Sm and ZnO:Er samples. The decrease in crystallite size for Er_xZnO_{1-x} and Sm_xZnO_{1-x} could be due to the evolution of the Er-O-Zn and Sm-O-Zn to the surface hindering the crystal growth. Since the ionic radius of Er^{3+} and Sm^{3+} is slightly higher than that of $Zn^{2+,}$ there is a slight distortion of the crystal lattice during the substitution after doping. At the same time, there is an observed increase in the lattice strain as shown in Figure 3 (b).

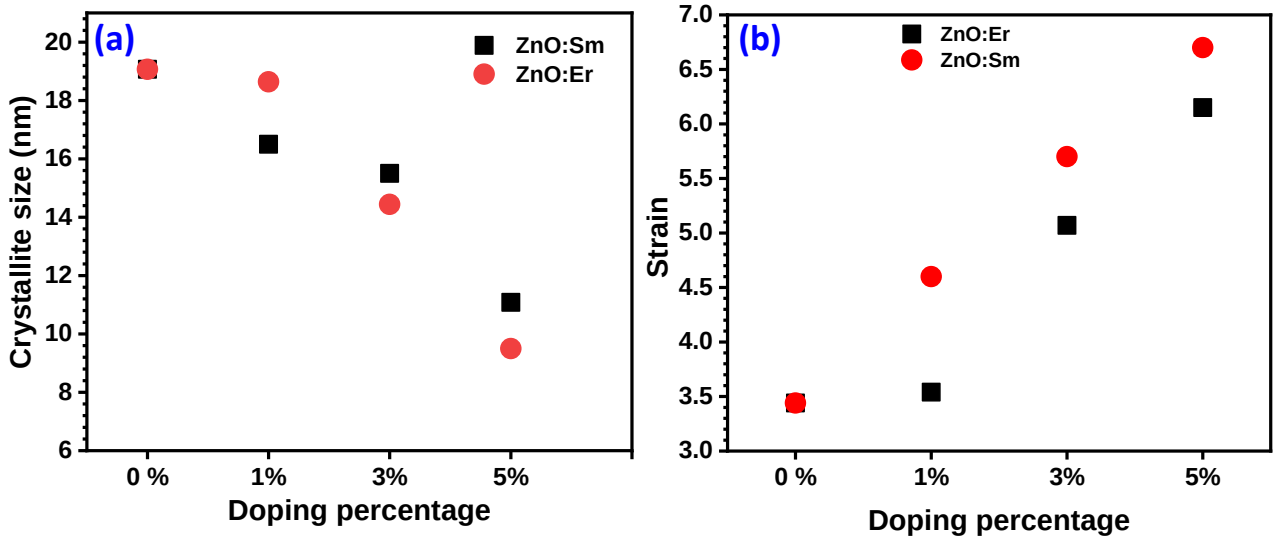

Figure 3. (a) Variation of the crystallite size and the doping percentage for Er_xZnO_{1-x} and Sm_xZnO_{1-x} samples

The increase in the lattice strain can also be another factor that hinders crystal growth. The enhancement of the lattice strain and the decrease in the crystallite size presents some defects in the ZnO lattice as a result of doping. A similar trend has been reported by Kayani *et al.* in their study of properties of Sm doped ZnO thin films [37]. During the doping process, a higher restricting force than the driving force on the grain boundaries is delivered by the dopants (Sm and Er). This restricting force hinders the growth of the grain boundary reducing the crystallite size with the increase in the dopant percentage. The obtained result in this study is consistent with Anand *et al.* on their study on the Sm doped codoped with AlZnO for optoelectronic applications [38].

Raman spectroscopy was conducted to study the effect of Sm and Er doping on vibrational properties of nanostructured ZnO as shown in Figure 4. The wurtzite hexagonal structure of ZnO belongs to $P6_{3mc}$ symmetry group with two formula units per primitive cell [39]. Based on group theory, the Raman active modes for ZnO are $A_1+E_1+2E_2$. In addition, the A_1 and E_1 phonon modes are polar and split into transverse and longitudinal. The peak at 438 cm^{-1} from Figure 4 is assigned to the high frequency of E_2 low mode of ZnO. This is the main peak for hexagonal wurtzite ZnO structure. The E_1 peak is further sensitive to internal stress and associated with the motion of oxygen atoms [40]. The peak observed between 576 cm^{-1} and 590 cm^{-1} wavenumbers for both undoped and doped ZnO is assigned to A_1 longitudinal optical (LO) phonon mode. The changes in the free carrier concentrations of ZnO are associated with this mode [41]. In addition, the peak is also associated with the Vo and Zn_i defects in ZnO [42]. The 331 cm^{-1} peak is associated with the second-order vibration of modes that are arising to E_2 (low) from E_2 (high) scattering process [43]. The peak at 100 cm^{-1} is assigned to the E_{2L} fundamental modes of wurtzite hexagonal ZnO. The 375cm^{-1} and 401 cm^{-1} modes which were less intense peaks are assigned to the A_1 transverse optical (TO) and E_1 (TO) phonon modes, which matches the vibration of O and Zn atoms in perpendicular and parallel to the c-axis of the structure of ZnO [44]. The low intensity of the A1 (LO) and E_1(LO) peaks is a result of a large number of defect states in ZnO hence can be a useful material in optoelectronic, sensing and photocatalysis applications [45]. However, for the ZnO:Er samples (Figure 4 a), there were two additional modes at 160 cm^{-1}, and 620 cm^{-1} that were observed to be dominant compared to the vibrational modes of ZnO. The substitution of Er in the ZnO which is the host could have resulted in the local vibration, leading to these modes. Similar modes have

been reported by Zamiri *et al.* on the optical and dielectric properties of Er-doped ZnO nanoplates [46].

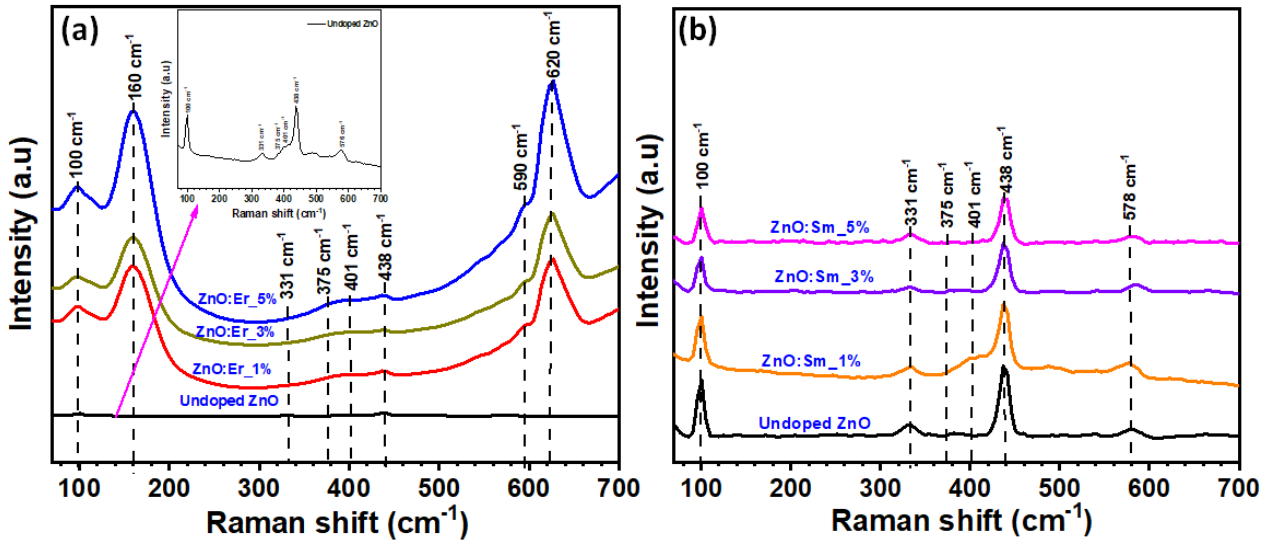

Figure 4. Raman vibrational modes of (a) ZnO:Er, and (b) ZnO:Sm samples. The inset in (a) shows the vibrational mode of undoped ZnO which could not be seen on ZnO:Er

Figure 5 shows the surface morphology of the undoped, Er-doped and Sm-doped samples. All the images reveal nanoparticles that are well-shaped and dispersed uniformly on the surface. There seems to be agglomeration on both the undoped and doped ZnO which decreases with the increase in the dopant concentrations. The Er and Sm-doped ZnO samples were more porous compared to the undoped ZnO. The increase in porosity is quite beneficial for the improvement in the electrical properties of the prepared samples. The Er and Sm clustered nanoparticles are distributed on the ZnO lattice. The grain sizes are not uniform at all places on the sample hence ImageJ was used to estimate the average diameter (nm). The insets of Figure 5 shows the Gaussian fitting and histogram used to estimate the grain sizes.

The grain sizes were observed to vary with the doping concentration. The undoped ZnO had an average grain size of 31.24 ± 1.36 nm. The grain sizes for the ZnO:Er was 37.54 ± 1.21 nm, 35.54 ± 0.27 nm, and 57.59 ± 2.16 nm for 1%, 3%, and 5%, respectively. For the ZnO:Sm, 42.90 ± 0.62 nm, 35.54 ± 0.29 nm, and 52.77 ± 3.03 nm grain sizes were obtained for 1 wt%, 3 wt%, and 5 wt%, respectively. The agglomeration of the nanoparticles caused the variation of the grain sizes.

Saleem *et al*. have reported a similar trend on the characteristics and photovoltaic applications of Au-doped-ZnO-Sm nanoparticle films whereby there was an increase in the agglomeration as the Au and Sm dopants were increased [47].

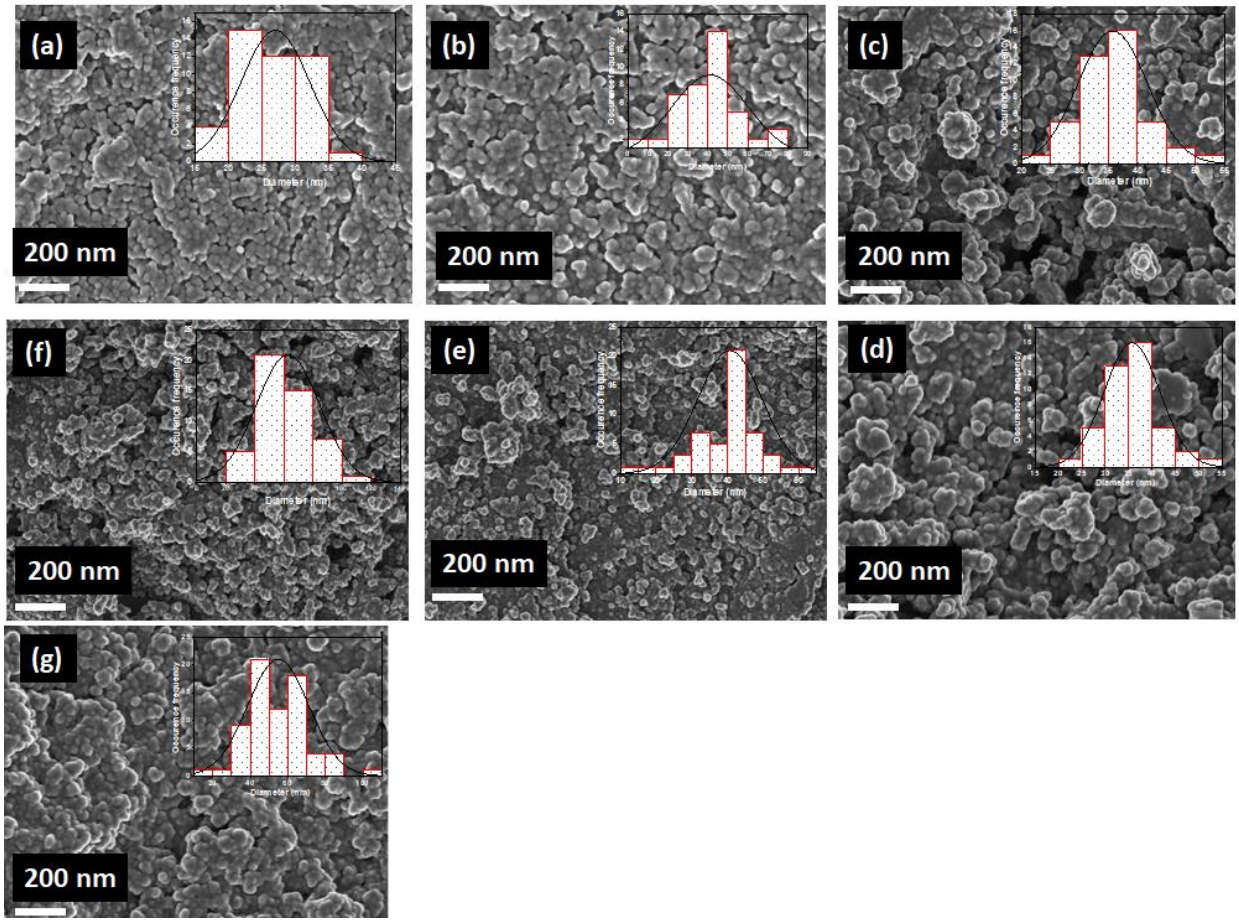

Figure 5. Surface morphology for the (a) undoped ZnO, (b-d) ZnO:Er, and (e-g) ZnO:Sm samples. The inset shows the Gaussian fitting and histogram estimated using ImageJ

EDX was used to study the elemental components for undoped ZnO, Er-doped and Sm-doped samples as shown in Figure 6. The inset on the EDX shows the color map obtained individually for all the samples. The EDX reveals the presence of Zn, Sm, Er and O in the samples. These signals (Zn, Sm, Er, and O) were predominant for all the samples. The sodium (Na) and calcium (Ca) signals, which comes from the soda-lime glass substrates used were present in all the samples. The carbon (C) signal that was used during the preparation of the samples was also present. The

EDX further reveal no other elements present, confirming the purity of the samples. The EDX results further confirm the purity of the undoped and doped samples.

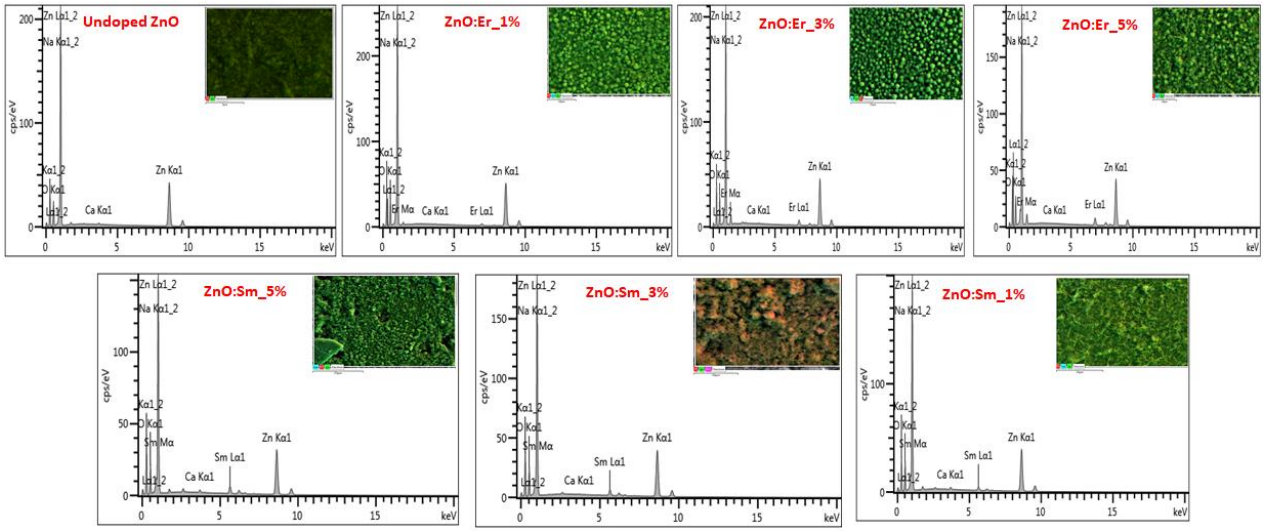

Figure 6. EDX analysis of undoped ZnO, ZnO:Sm, and ZnO:Er samples

3.3 Optical studies

Figure 7 shows the transmittance spectra for all the thin films as a function of wavelength (nm). The films exhibit good transmittance in the visible region. At the same time, high absorption in the wavelength that ranges from 350 to 400 nm can be observed since there was a sharp decrease in the transmittance. There was no observed shift in the absorption edge upon the incorporation of Sm and Er into the ZnO lattice. The average transmittance of 74 % at a wavelength of 650 nm for all the films was obtained. However, there is an observed decrease in transmittance as the dopants (Er and Sm) were increased. This could be due to an increase in thickness and surface roughness on the films. The defects in the films that normally occur in the wavelength that ranges from 300 to 370 nm were not observed in all the films, an indication of the crystallinity of the samples. Asikuzun *et al.* have reported a similar study on the properties of Er-doped ZnO thin films [48]. Equation 3 was used in the calculation of the absorption coefficient (α);

$$\alpha = \frac{1}{\tau} lnT \qquad 2$$

where *t* is the thickness and T is the transmittance of the thin films [48]. The optical bandgap (Eg) of the undoped, Sm doped and Er-doped films were thereafter obtained using Tauc's relation

$$\alpha h\nu = A(h\nu - E_g)^n \qquad 3$$

where α is the absorption coefficient, A is constant $h\nu$ is the photon energy, E_g and n depend on the nature of transition whereby it is ½ for allowed indirect transition, and 2 for allowed direct transition [30]. From Tauc's plot, the extrapolation of the linear portion to the $h\nu$ axis gives the bandgap of the films.

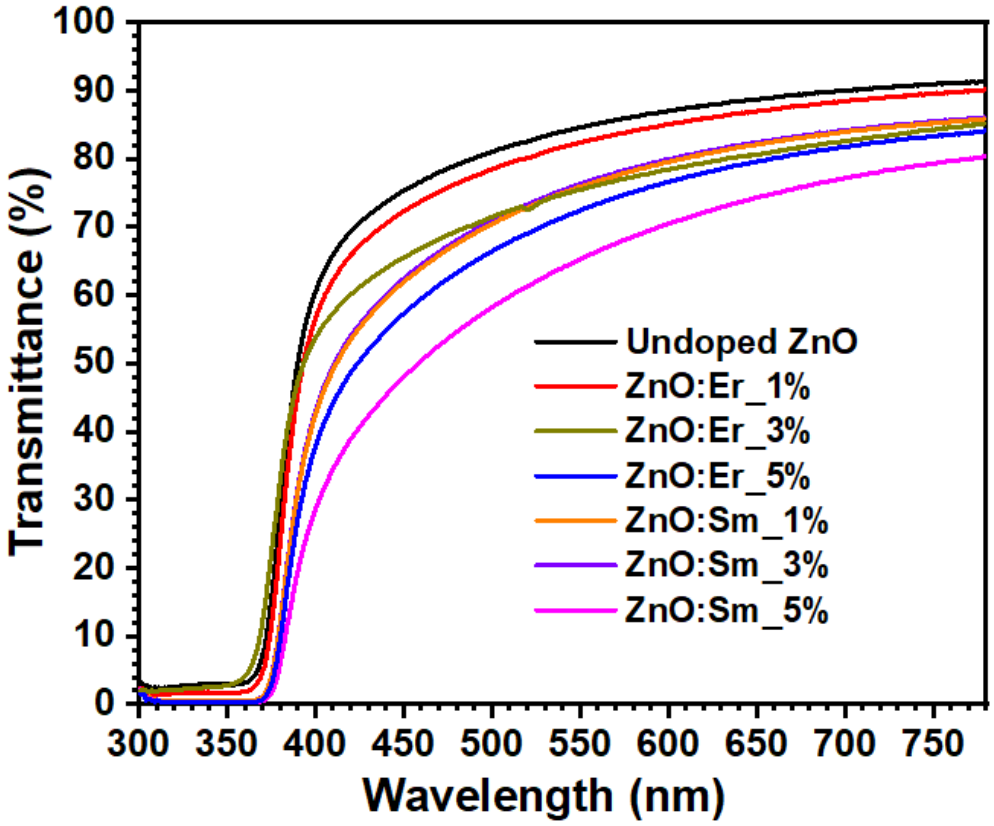

Figure 7. Transmittance spectra of the undoped ZnO, ZnO:Sm and ZnO:Er thin films

The optical bandgap for the undoped ZnO was 3.31 eV. For the ZnO:Er, 3.23, 3.21, and 2.96 eV were obtained for 1 wt%, 3 wt%, and 5 wt%, respectively. On the other hand, ZnO doped with Sm had an E_g of 3.27, 3.18, and 3.11 eV for 1 wt%, 3 wt%, and 5 wt%, respectively. There was an observed trend of the bandgap decrease for all the doped samples compared with the undoped

ZnO. This decrease in the bandgap is not due to the quantum confinement effect but rather the incorporation of additional states. During doping, additional states below the conduction band could have been formed, which might have led to the decrease in the bandgap of the Er and Sm doped ZnO thin films. Impurities, which are the dopants in this study can create energy levels in the bandgap near the band edges. Increasing the concentration of the dopants leads to an increase in the density of states forming continuum states which leads to the decrease in the energy bandgap. Different researchers have reported similar observations. Anand *et al.* in their study on rare earth of Sm codoped with Al on ZnO reported the general decrease in bandgap and associated it with the lattice defect present in their films [38]. Another study conducted by Zamiri *et al.* on the effects of rare-earth (Er, La, and Yb) doped with ZnO found out the decrease in the bandgap with the concentration of the dopant which was due to lower defect concentration of the pure ZnO crystals [49].

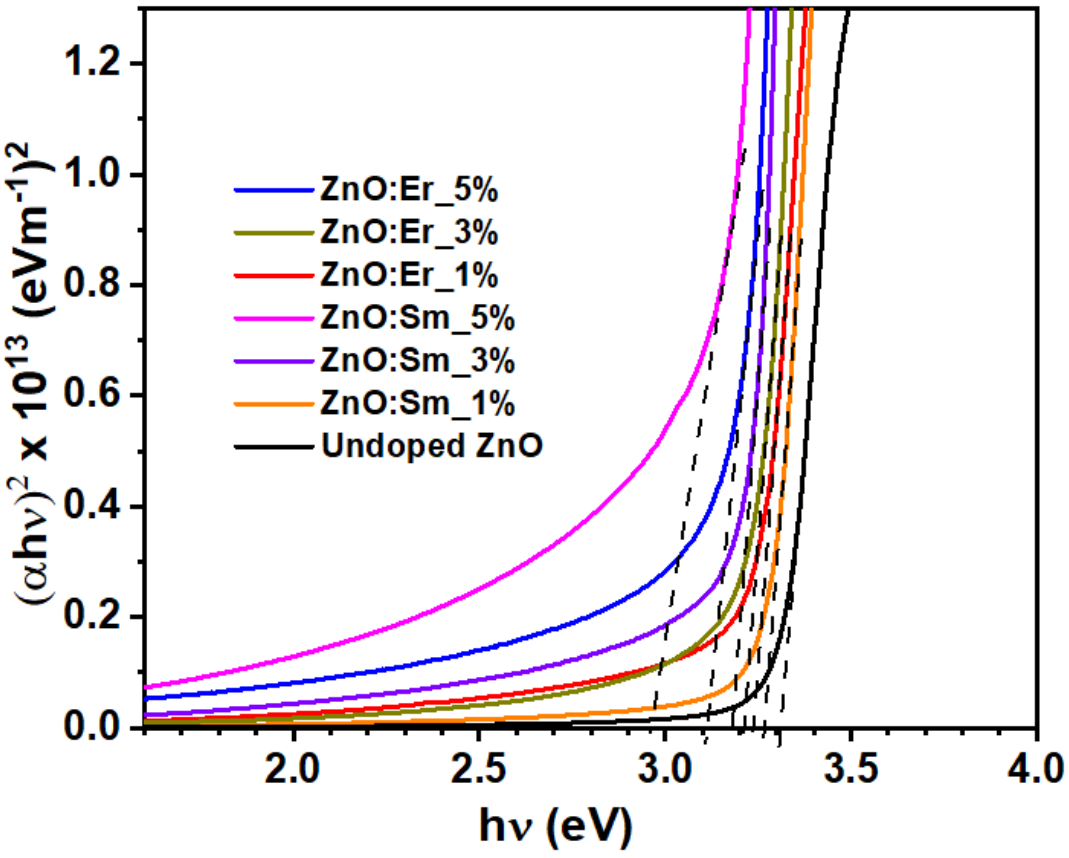

Figure 8. Energy bandgap for undoped, Er-doped and Sm-doped ZnO samples

3.3 Electrical properties

Figure 9 shows the *I-V* characteristics for the undoped, Sm-doped and Er-doped ZnO which is in semi-log scale. From the thermionic emission theory, *I-V* characteristics of the Schottky device with a series resistance R_s is given by equation 4 [29];

$$I = I_s\left[1 - \exp\left(\frac{-q(V-IR_s}{k_BT}\right)\right] \quad 4$$

where q is the electronic charge, R_s is the series resistance, k_B is the Boltzmann constant, T is the absolute temperature, I_s is the saturation current which is given by [6];

$$I_s = SA^*T^2\exp(-\frac{q\phi_{B0}}{nk_BT}) \quad 5$$

where A is the Richardson constant, ϕ_{B0} is the zero-bias Schottky barrier height, S is the contact area of the metal diode and n which is the ideality factor. These values were determined from the linear region of the *I-V* characteristics using equation 6 [6, 17];

$$n = \frac{q}{k_BT}\left[\frac{\Delta V}{\Delta lnI}\right] \quad 6$$

From the curves, there was an improvement in the rectification behavior for the doped samples from the undoped ZnO. The 5 wt% Er and Sm-doped ZnO samples have a rectification of almost 4 orders of magnitude compared to 2 orders of magnitude for the undoped ZnO. 1wt% and 3 wt% of Er and Sm doped samples on the other hand had an improvement in the rectification behavior of 3 orders of magnitude. The better rectification for the doped samples indicates an improvement in the Schottky behavior of these devices.

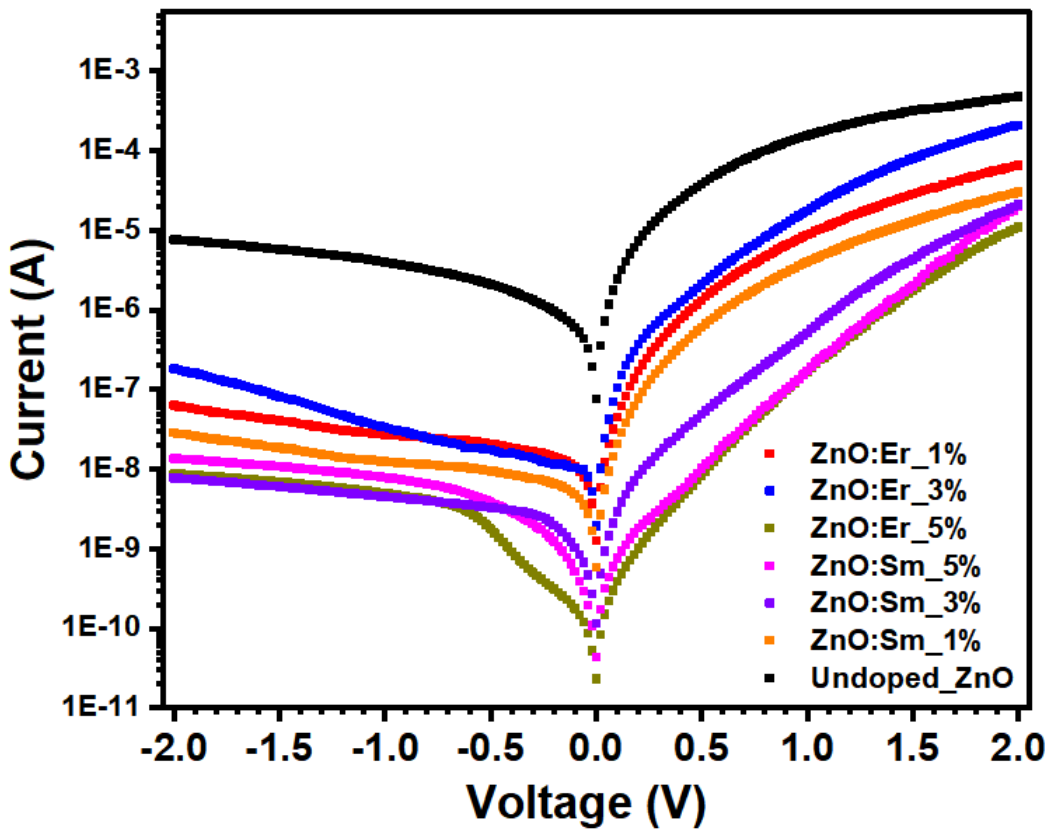

Figure 9. *I-V* characteristics of Pd/ZnO/p-Si/Al-Au Schottky diodes for undoped, Sm-doped and Er-doped ZnO thin films

The saturation current values for the Schottky diodes were obtained by extrapolation of the linear part of the *I-V* curve. Table 1 gives summarizes the Schottky diode parameters; the ideality factor, saturation current, and series resistance. From Table 1, ϕ_{B0} for undoped ZnO was 0559. There is an observed increase of the ϕ_{B0} from 0.652 for 1 wt % doped Sm to 0.760 for 5 wt% doped ZnO samples, while for Er-doped ZnO, a decrease of ϕ_{B0} from 0.636 to 0.767 was obtained for 1 wt% and 5 wt% samples, respectively.

Table 1. Summary of the Schottky barrier heights, ideality factor, leakage current and series resistance for undoped, Er-doped and Sm-doped ZnO Schottky devices

Device	ϕ_{B0} (eV)	n	I_s (A)	R_s (kΩ)
Undoped ZnO	0.559	2.49	2.15×10^{-7}	31.470
ZnO:Sm_1%	0.652	1.95	5.72×10^{-9}	19.145
ZnO:Sm_3%	0.728	1.84	2.96×10^{-9}	13.217
ZnO:Sm_5%	0.760	1.71	8.44×10^{-11}	2.562
ZnO:Er_1%	0.636	2.43	1.08×10^{-8}	14.883
ZnO:Er_3%	0.652	2.08	6.83×10^{-9}	10.481
ZnO:Er_5%	0.767	1.92	6.48×10^{-11}	3.141

The undoped ZnO had an ideality factor of 2.49. The ideality factor decreased with the increase of the dopant with the lowest ideality factor of 1.71 and 1.92 obtained for 5 wt% Sm and Er-doped ZnO samples, respectively as shown in Figure 10. However, the obtained ϕ_{B0} was higher than the actual theoretical values and this could be due to the barrier tunneling and the defects created both for the undoped and doped samples [18]. Also, the films could be inhomogeneous at the interface barrier height. A study by Brillson *et al.* has shown that the barrier height can also be affected by the dielectric for the films prepared using solution-based methods [50]. The *I-V* results in this study indicate that the ideality factor obtained is non-ideal since ideal diodes have an ideality factor of 1. The non-ideal diode obtained instead of ideal could be due to voltage drop across the metal/semiconductor interface and high series resistance. This study is consistent with a study conducted by Ahmed *et al.* whereby they obtained a comparable ideality factor of 0.66 [14]. Er and Sm-doped with ZnO obtained from this study can therefore be used as diodes. There was a decrease in the leakage current with the increase in the dopant concentration as shown in Table 1, a further confirmation of the improvement in the rectification behavior.

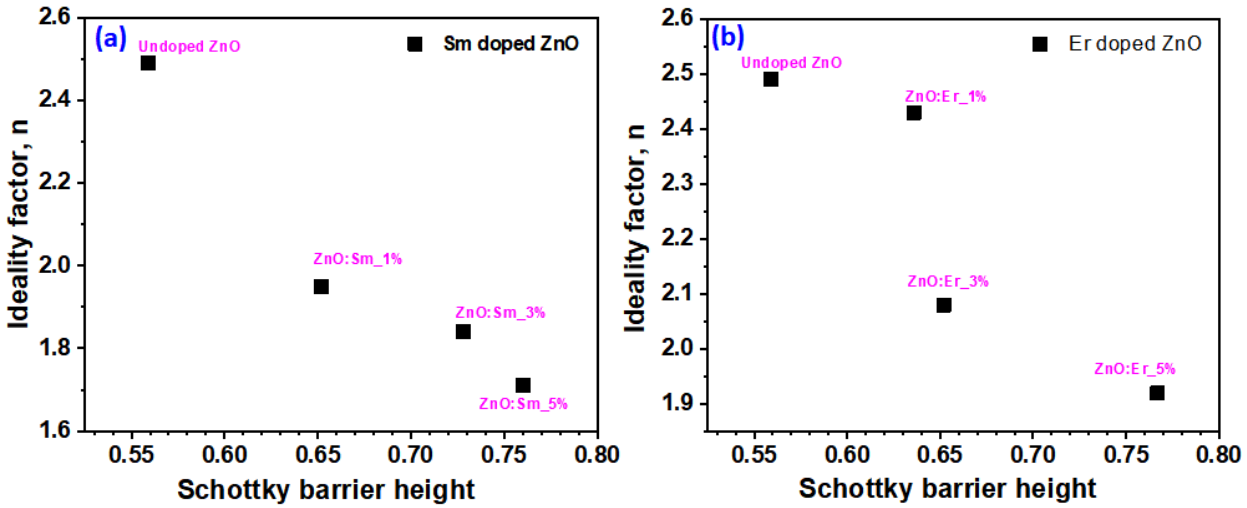

Figure 10. Relationship between the ideality factor and Schottky Barrier height for (a) Sm-doped and (b) Er-doped ZnO thin films

For a better understanding of the carrier transport mechanisms in our Schottky diodes, the lin of current (*I*) against voltage (*V*) was plotted as shown in Figure 11. Two different mechanisms shown by regions *a* and *b* can be seen in all the films. The devices show an Ohmic behavior at low voltage (region a). The transport mechanism in this region is due to the tunneling of the charge carriers between states at the interface. On the other hand, the current is exponentially related to the voltage in region b. This transport mechanism in this region is due to the recombination tunneling. A similar observation has been reported by Hwang *et al.* in their study on non-surface treated Au/ZnO Schottky diodes [51].

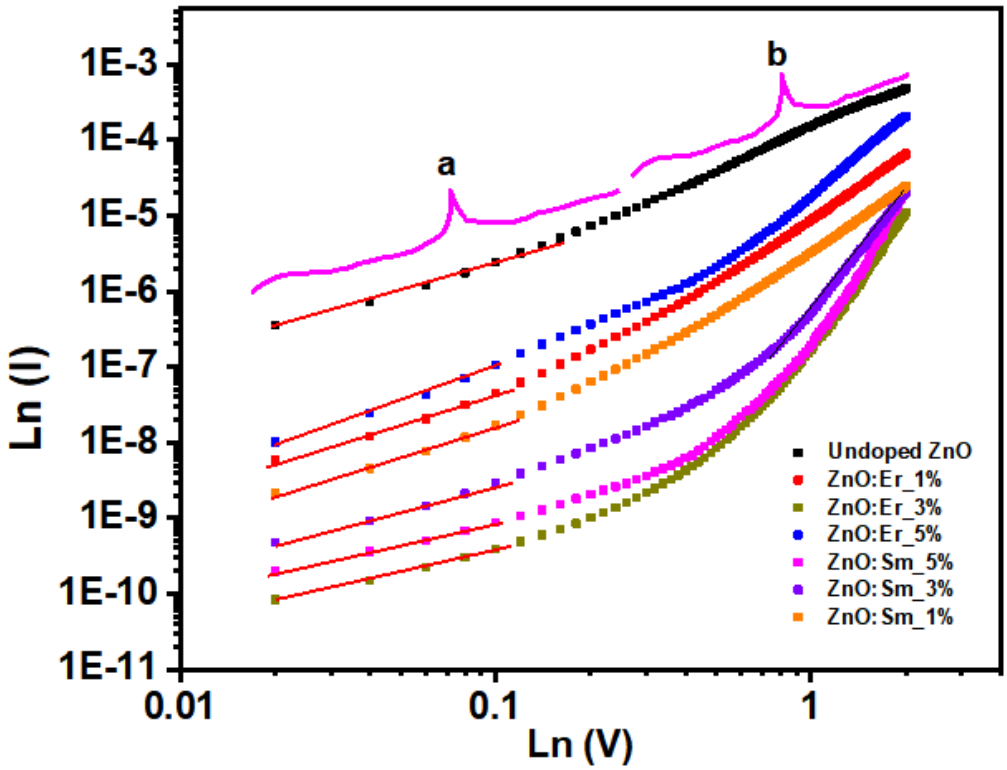

Figure 11. A plot of ln *I* against ln *V* for undoped, Sm-doped and Er-doped ZnO Schottky devices

4.0 Conclusion

In this study, undoped, Sm-doped and Er-doped ZnO thin films were successfully synthesized on soda-lime glass and p-Si using spray pyrolysis. The effect of doping on morphological, structural, optical and electrical properties were thereafter studied. XRD studies revealed the main planes associated with wurtzite hexagonal ZnO indexed in their right 2-theta angles, both for undoped and doped samples. However, a shift to the lower 2theta angles was observed due to the Er^{3+} and Sm^{3+} that were incorporated into the Zn^{2+} lattice. The sharp peaks indicate the crystallinity of the synthesized samples. Raman spectroscopy observed A_1, E_1, and E_2 which are the main phonon modes of ZnO. The 438 cm^{-1} which is the main mode associated with the wurzite hexagonal ZnO was assigned to E_2 (low) mode. The mode that ranged from 576 to 590 cm^{-1} is assigned to A_1 and was associated with V_o and Zn_i defects in ZnO. For Er-doped ZnO, there were two intense modes at 160 cm^{-1} and 620 cm^{-1}. These modes were due to local vibration during the substitution of Er

into ZnO lattice. The SEM studies revealed nanoparticles uniformly distributed on the surface with some agglomeration on the doped ZnO. The agglomeration was decreasing with an increase in dopant concentration. Also, there was an improvement in the porosity for the doped ZnO. Average grain sizes that ranged from 31.24 to 57.77 nm were obtained for all the samples. EDX confirmed the purity of the samples with the main signals of Er, Sm, Zn, and O present. The films were transmitting highly in the visible region and absorbed in the UV region. There was a general decrease in the bandgap with the increase in the dopant concentration ranging from 3.31 eV to 2.96 eV. From the *I-V* measurements, there was an improvement in the electrical behavior of the doped samples compared with undoped ZnO. 5 wt% Er and Sm doped ZnO had almost 4 orders of rectification compared to 2 orders for undoped ZnO. The Schottky increased with an increase in the doping concentration while the ideality factor, saturation current and series resistance decreased. From this study, there Er and Sm doped ZnO can therefore be used as alternative Schottky devices.

Acknowledgement.

The authors wish to thank the Department of Physics, the University of Pretoria for support and externally Funded UP Post-Doctoral Fellowship Programme: Grant Cost Centre N0115/115463 of the SARChI.

References

1. El Haimeur, A., et al., *Reducing p-type Schottky contact barrier in metal/ZnO heterostructure through Ni-doping.* Applied Surface Science, 2021. **545**: p. 149023.
2. Salem, K.E., et al., *Ge-doped ZnO nanorods grown on FTO for photoelectrochemical water splitting with exceptional photoconversion efficiency.* International Journal of Hydrogen Energy, 2021. **46**(1): p. 209-220.
3. Nyarige, J.S., et al., *Structural and optical properties of phosphorous and antimony doped ZnO thin films deposited by spray pyrolysis: a comparative study.* 2017.
4. Deng, X., et al., *ZnO enhanced NiO-based gas sensors towards ethanol.* Materials Research Bulletin, 2017. **90**: p. 170-174.
5. Namini, A.S., et al., *Synthesis and characterization of novel ZnO/NiCr2O4 nanocomposite for water purification by degradation of tetracycline and phenol under visible light irradiation.* Materials Research Bulletin, 2021. **139**: p. 111247.

6. Mwankemwa, B.S., et al., *tructural, morphological, optical and electrical properties of Schottky diodes based on CBD deposited ZnO: Cu nanorods.* Superlattices and Microstructures, 2017. **107**: p. 163-171.
7. Hwang, J.-D. and Z.-J. Hong, *Enhancing the Schottky-barrier height by inserting a thin MgO layer between Au and annealed-ZnO.* Materials Research Bulletin, 2021. **144**: p. 111478.
8. Wu, T.-H., et al., *UV photocurrent responses of ZnO and MgZnO/ZnO processed by atmospheric pressure plasma jets.* Journal of Alloys and Compounds, 2015. **628**: p. 68-74.
9. Cheng, G., et al., *ZnO nanowire Schottky barrier ultraviolet photodetector with high sensitivity and fast recovery speed.* Applied Physics Letters, 2011. **99**(20): p. 203105.
10. Boruah, B.D., *Zinc oxide ultraviolet photodetectors: rapid progress from conventional to self-powered photodetectors.* Nanoscale Advances, 2019. **1**(6): p. 2059-2085.
11. Ali, G.M., *Performance analysis of planar Schottky photodiode based on nanostructured ZnO thin film grown by three different techniques.* Journal of Alloys and Compounds, 2020. **831**: p. 154859.
12. Mokrushin, A.S., et al., *Chemoresistive gas-sensitive ZnO/Pt nanocomposites films applied by microplotter printing with increased sensitivity to benzene and hydrogen.* Materials Science and Engineering: B, 2021. **271**: p. 115233.
13. Chankhanittha, T., et al., *Silver decorated ZnO photocatalyst for effective removal of reactive red azo dye and ofloxacin antibiotic under solar light irradiation.* Colloids and Surfaces A: Physicochemical and Engineering Aspects, 2021: p. 127034.
14. Ahmed, M., W.E. Meyer, and J.M. Nel, *Structural, optical and electrical properties of the fabricated Schottky diodes based on ZnO, Ce and Sm doped ZnO films prepared via wet chemical technique.* Materials Research Bulletin, 2019. **115**: p. 12-18.
15. Zhang, L., et al., *Effects of the Er2O3 doping on the microstructure and electrical properties of ZnO–Bi2O3 based varistor ceramics.* Ceramics International, 2021. **47**(22): p. 32349-32356.
16. Gozeh, B.A., et al., *Solar light responsive ZnO nanoparticles adjusted using Cd and La Co-dopant photodetector.* Journal of Alloys and Compounds, 2018. **732**: p. 16-24.
17. Khan, M.A., et al., *ZnO nanowires based schottky contacts of Rh/ZnO interfaces for the enhanced performance of electronic devices.* Surfaces and Interfaces, 2020. **21**: p. 100649.
18. Amin, G., et al., *Current-transport studies and trap extraction of hydrothermally grown ZnO nanotubes using gold Schottky diode.* physica status solidi (a), 2010. **207**(3): p. 748-752.
19. Yang, Y., et al., *High-performance piezoelectric gate diode of a single polar-surface dominated ZnO nanobelt.* Nanotechnology, 2009. **20**(12): p. 125201.
20. Kaufmann, I.R., et al., *A Study about Schottky Barrier Height and Ideality Factor in Thin Film Transistors with Metal/Zinc Oxide Nanoparticles Structures Aiming Flexible Electronics Application.* Nanomaterials, 2021. **11**(5): p. 1188.
21. Zheng, Z., et al., *High-performance flexible UV photodetector based on self-supporting ZnO nano-networks fabricated by substrate-free chemical vapor deposition.* Nanotechnology, 2021. **32**(47): p. 475201.
22. Mostafa, A.M., et al., *Linear and nonlinear optical studies of Ag/Zn/ZnO nanocomposite thin film prepared by pulsed laser deposition technique.* Radiation Physics and Chemistry, 2021. **179**: p. 109233.

23. Ayouchi, R., et al., *Growth of pure ZnO thin films prepared by chemical spray pyrolysis on silicon.* Journal of Crystal Growth, 2003. **247**(3-4): p. 497-504.
24. Abdulrahman, A.F., et al., *Effect of growth temperature on morphological, structural, and optical properties of ZnO nanorods using modified chemical bath deposition method.* Journal of Electronic Materials, 2021. **50**(3): p. 1482-1495.
25. Gegova-Dzhurkova, R., et al., *Modification of surface morphology and lattice order in nanocrystalline ZnO thin films prepared by spin-coating sol–gel method.* Journal of Sol-Gel Science and Technology, 2021. **100**(1): p. 55-67.
26. Saravanakumar, B., R. Mohan, and S.-J. Kim, *Facile synthesis of graphene/ZnO nanocomposites by low temperature hydrothermal method.* Materials Research Bulletin, 2013. **48**(2): p. 878-883.
27. Zhao, Y., et al., *Preparation and gas-sensitive properties of litchi shell-like NiO film modified porous ZnO composite by electrodeposition method.* Sensors and Actuators A: Physical, 2021. **320**: p. 112574.
28. Al Farsi, B., et al., *Structural and optical properties of visible active photocatalytic Al doped ZnO nanostructured thin films prepared by dip coating.* Optical Materials, 2021. **113**: p. 110868.
29. Ahmed, M., et al., *Effect of Sm doping ZnO nanorods on structural optical and electrical properties of Schottky diodes prepared by chemical bath deposition.* Materials Science in Semiconductor Processing, 2018. **79**: p. 53-60.
30. Nyarige, J.S., T.P. Krüger, and M. Diale, *Structural and optical properties of hematite and L-arginine/hematite nanostructures prepared by thermal spray pyrolysis.* Surfaces and Interfaces, 2020. **18**: p. 100394.
31. Nyarige, J.S., T.P. Krüger, and M. Diale, *Effects of L-arginine concentration on hematite nanostructures synthesized by spray pyrolysis and chemical bath deposition.* Physica B: Condensed Matter, 2020. **581**: p. 411924.
32. Nyarige, J.S., T.P. Krüger, and M. Diale, *Influence of precursor concentration and deposition temperature on the photoactivity of hematite electrodes for water splitting.* Materials Today Communications, 2020. **25**: p. 101459.
33. Farhat, S., M. Rekaby, and R. Awad, *Synthesis and characterization of Er-doped nano ZnO samples.* Journal of Superconductivity and Novel Magnetism, 2018. **31**(9): p. 3051-3061.
34. Kumar, K.D.A., et al., *Effect of Er doping on the ammonia sensing properties of ZnO thin films prepared by a nebulizer spray technique.* Journal of Physics and Chemistry of Solids, 2020. **144**: p. 109513.
35. Najim, J. and J. Rozaiq, *Effect Cd doping on the structural and optical properties of ZnO Thin Films.* International Letters of Chemistry, Physics and Astronomy, 2013. **10**: p. 137-150.
36. Li, G., et al., *Doping and annealing effects on ZnO: Cd thin films by sol–gel method.* Journal of Alloys and Compounds, 2011. **509**(14): p. 4816-4823.
37. Kayani, Z.N., et al., *Enhanced magnetic, antibacterial and optical properties of Sm doped ZnO thin films: Role of Sm doping.* Optical Materials, 2020. **108**: p. 110457.
38. Anand, V., et al., *Rare earth Sm3+ co-doped AZO thin films for opto-electronic application prepared by spray pyrolysis.* Ceramics International, 2018. **44**(6): p. 6730-6738.
39. Jayachandraiah, C. and G. Krishnaiah, *Erbium induced raman studies and dielectric properties of Er-doped ZnO nanoparticles.* Adv. Mater. Lett, 2015. **6**(8): p. 743-748.

40. Duan, L., et al., *Magnetization and Raman scattering studies of (Co, Mn) codoped ZnO nanoparticles.* Journal of Applied Physics, 2008. **104**(1): p. 013909.
41. Romčević, N., et al., *Raman scattering from ZnO incorporating Fe nanoparticles: vibrational modes and low-frequency acoustic modes.* Journal of alloys and compounds, 2010. **507**(2): p. 386-390.
42. Tseng, Y.-C., et al., *Dependence of luminescent properties and crystal structure of Li-doped ZnO nanoparticles upon Li content.* Journal of luminescence, 2012. **132**(8): p. 1896-1899.
43. Choudhary, S., et al., *Rapid synthesis of ZnO nanowires and nanoplates with highly enhanced photocatalytic performance.* Applied Surface Science, 2021. **541**: p. 148484.
44. Cuscó, R., et al., *Temperature dependence of Raman scattering in ZnO.* Physical Review B, 2007. **75**(16): p. 165202.
45. Kumar, N., et al., *Morphogenesis of ZnO nanostructures: role of acetate (COOH−) and nitrate (NO 3−) ligand donors from zinc salt precursors in synthesis and morphology dependent photocatalytic properties.* RSC Advances, 2015. **5**(48): p. 38801-38809.
46. Zamiri, R., et al., *Er doped ZnO nanoplates: synthesis, optical and dielectric properties.* Ceramics International, 2014. **40**(1): p. 1635-1639.
47. Saleem, M., et al., *Characteristics and Photovoltaic Applications of Au-Doped ZnO–Sm Nanoparticle Films.* Nanomaterials, 2021. **11**(3): p. 702.
48. Asikuzun, E., et al., *High-quality c-axis oriented non-vacuum Er doped ZnO thin films.* Ceramics International, 2016. **42**(7): p. 8085-8091.
49. Zamiri, R., et al., *Effects of rare-earth (Er, La and Yb) doping on morphology and structure properties of ZnO nanostructures prepared by wet chemical method.* Ceramics international, 2014. **40**(1): p. 523-529.
50. Brillson, L.J. and Y. Lu, *ZnO Schottky barriers and Ohmic contacts.* Journal of Applied Physics, 2011. **109**(12): p. 8.
51. Hwang, J.-D., C.-Y. Kung, and Y.-L. Lin, *Non-surface-treated Au/ZnO Schottky diodes using pre-annealed hydrothermal or sol-gel seed layer.* IEEE transactions on nanotechnology, 2012. **12**(1): p. 35-39.